Comprehensive Studies of Magnetic Transitions and Spin-Phonon Couplings in the Tetrahedral Cobalt Complex $Co(AsPh_3)_2I_2$

Duncan H. Moseley,[a] Zhiming Liu,[a] Alexandria N. Bone,[a] Shelby E. Stavretis,[a] Saurabh Kumar Singh,[b] Mihail Atanasov,[c,d,*] Zhengguang Lu,[e] Mykhaylo Ozerov,[e] Komalavalli Thirunavukkuarasu,[f] Yongqiang Cheng,[g] Luke L. Daemen,[g] Daphné Lubert-Perquel,[e] Dmitry Smirnov,[e] Frank Neese,[c] A. J. Ramirez-Cuesta,[g] Stephen Hill,[e,h] Kim R. Dunbar,[i] Zi-Ling Xue[a,*]

[a] *Department of Chemistry, University of Tennessee, Knoxville, Tennessee 37996, United States*

[b] *Department of Chemistry, Indian Institute of Technology Hyderabad, Kandi-502285, Sangareddy, Telangana, India*

[c] *Max Planck Institute for Coal Research, Kaiser-Wilhelm-Platz 1, D-45470 Mülheim an der Ruhr, Germany*

[d] *Institute of General and Inorganic Chemistry, Bulgarian Academy of Sciences, 1113 Sofia, Bulgaria*

[e] *National High Magnetic Field Laboratory, Florida State University, Tallahassee, Florida 32310, United States*

[f] *Department of Physics, Florida A&M University, Tallahassee, Florida 32307, United States*

[g] *Neutron Scattering Division, Oak Ridge National Laboratory, Oak Ridge, Tennessee 37831, United States*

[h] *Department of Physics, Florida State University, Tallahassee, Florida 32306, United States*

[i] *Department of Chemistry, Texas A&M University, College Station, Texas 77843, United States*

Abstract

A combination of inelastic neutron scattering (INS), far-IR magneto- (FIRMS) and Raman magneto-spectroscopies (RaMS) have been used to comprehensively probe magnetic excitations in $Co(AsPh_3)_2I_2$ (**1**), a reported single-molecule magnet (SMM). With applied field, magnetic zero-field splitting (ZFS) peak ($2D'$) shifts to higher energies in each spectroscopy. INS placed the ZFS peak at 54 cm^{-1}, as revealed by both variable-temperature (VT) and variable-magnetic-field data, giving results that agree well with those from both far-IR and Raman studies. Both FIRMS and Raman magneto-spectra also reveal the presence of multiple spin-phonon couplings as avoided crossings with neighboring phonons. Here, phonons refer to both intramolecular and lattice vibrations. The results constitute a rare case in which the spin-phonon couplings are observed with both Raman-active (*g* modes) and far-IR-active phonons (*u* modes; space group $P2_1/c$, No. 14, $Z = 4$ for **1**). These couplings are fit using a simple avoided crossing model with coupling constants of ~1-2 cm^{-1}. The combined spectroscopies accurately determine the magnetic excited level and the interaction of the magnetic excitation with phonon modes. Density functional theory (DFT) phonon calculations compare well with INS, allowing for the assignment of the modes and their symmetries. Electronic calculations elucidate the nature of ZFS in the complex. Features of different techniques to determine ZFS and other spin-Hamiltonian parameters in transition metal complexes are summarized.

Introduction

Single-molecule magnets (SMMs) with slow spin relaxation from one ground state to another have been actively studied as potential, new data storage materials.[1-13] Ideally, the primary relaxation mechanism would be to traverse the energy barrier separating the two

states.[4,14-16] However, other processes, such as spin-lattice relaxations (i.e., spin-phonon coupling) and quantum tunneling, often complicate the relaxation processes.[1-4] These mechanisms are still poorly understood. In addition, direct determination of the barrier height is essential. For d metal complexes with quenched angular momenta, the barrier is defined by the magnitude of zero-field splitting (ZFS) with axial (D) and rhombic (E) anisotropic parameters.[16]

Magnetic properties of $Co(AsPh_3)_2I_2$ (**1**) were previously studied by Saber and Dunbar, showing slow magnetic relaxation in **1** with easy-axis ZFS (D = -74.7 cm^{-1}, E = -0.82 cm^{-1}) from magnetometric studies.[17] The axial anisotropy is a significant increase compared to its phosphine analogs $Co(PPh_3)_2X_2$ (X = Cl, Br, I).[17-19] Magnetometry is a bulk, non-resonant method.[4] Parameters from the technique are often prone to large errors.

A common method for directly determining ZFS parameters is high-field EPR (HFEPR).[4] HFEPR is highly accurate, but is often limited to energies of <33 cm^{-1}, with few exceptions.[20-21] It was used, e.g., in studies of $Co(PPh_3)_2Cl_2$, yielding its spin-Hamiltonian parameters (i.e., D, E, g_x, g_y and g_z).[22] Far-IR magneto-spectroscopy (FIRMS) can easily reach much higher energies and has become more commonly used.[23-29] This method is very useful for observing magnetic-dipole allowed ZFS transitions.[30] The main issue with interpreting FIRMS spectra versus EPR spectra is the prevalence of phonons in FIRMS, making the use of magnetic fields necessary.[31] Much of the work using FIRMS to study SMMs has been reported by van Slageren and coworkers,[23,28-29] showing FIRMS as a direct method to observe magnetic barriers.[25-26,32-35]

Another method with very few uses for observing ZFS transitions is Raman magneto-spectroscopy (RaMS). It has only been used to determine magnetic levels in two transition metal compounds,[25,36] while other complexes have been attempted by us, showing no observed magnetic transitions in RaMS. In the study of $Fe(H_2O)_6{\cdot}SiF_6$ by Gnezdilov and coworkers, the

transitions were directly observed as clear individual Raman peaks split with field.[36] The high-spin d^6, O_h $Fe^{II}(H_2O)_6 \cdot SiF_6$ likely has first-order spin-orbit coupling (SOC), probably making the Raman peaks with significant contributions from electronic transitions.[37-38] In the high-spin d^7 complex $Co(acac)_2(H_2O)_2$, first-order SOC is, however, quenched. In RaMS studies of $Co(acac)_2(H_2O)_2$, the transition between the ZFS states was only observed when it is in close proximity to neighboring Raman-active (*g* symmetry) phonon peaks, effectively taking the intensity of the phonon peaks by an avoided crossing mechanism.[25] In FIRMS studies of $Co(acac)_2(H_2O)_2$, the magnetic-dipole-allowed ZFS transitions were observed, although they do not undergo spin-phonon couplings with IR-active (*u* symmetry) phonon peaks.[25] Currently, the Raman-selection rules about ZFS transitions are not well understood, requiring further studies.

Inelastic neutron scattering (INS) is a powerful method for probing magnetic energy levels and phonons in *d* and *f* complexes[39-44] with increasing uses recently.[25-26,31,45-52] INS, covering a variety of methods and spectrometers, has been reviewed.[42,53] As in FIRMS, finding a magnetic peak among phonon peaks in INS spectra is often a challenge. INS may directly reveal magnetic transitions, especially when few phonons are nearby.[31,50-51] When magnetic peaks overlap with phonons, VT or variable-field INS may be used to reveal the magnetic peaks. The former, followed by Bose-correction (to bring peaks of phonons, which are Bosons, at different temperatures to a similar level), may show magnetic peaks (from electrons, which are Fermions).[32,42] Here, calculated INS spectrum of phonons may help reveal the magnetic peaks. The latter applies magnetic fields, shifting magnetic transitions, while phonons are unaffected by magnetic fields unless there is spin-phonon coupling. To date, magnetic fields have only sparingly been used for inter-Kramers doublet (KD) transitions in SMMs.[32,48-49]

Spin-phonon coupling in SMMs is the primary mechanism for magnetic relaxation, often

relying on the direct or Raman mechanisms.[54] In recent years, the couplings between the excited magnetic peak and neighboring phonons have been directly observed in both *d* and *f* complexes.[23,25-26,48,55-56] In many cases, these couplings can be fit to a simple spin-phonon coupling model and present coupling constants of ~1-3 cm^{-1}, the nature of which is under investigation by theory.[9,57-66]

Herein, we present a comprehensive spectroscopic study of $Co(AsPh_3)_2I_2$ (**1**) to evaluate the inter-KD ZFS transition $M_S = \pm 3/2 \rightarrow \pm 1/2$ by a combination of FIRMS, RaMS and INS assisted by phonon calculations. The magnetic peak is clearly visible by all three methods, displaying spin-phonon couplings in the form of avoided crossings in both FIRMS and RaMS. Several techniques to probe magnetic properties of transition metal complexes are summarized in a table at the end of Results and Discussion.

Results and Discussion

Structure of **1** is given in Figure 1,[17] showing molecular (or local) symmetry of approximately C_{2v} which will be used to discuss its magnetic transitions. In a $D < 0$ system, expected transitions stem from the ground state $M_S = \pm 3/2$ ($E = 0$) or mixed state $\phi_{1,2}$ ($E \neq 0$; Figure 1).[67-68] Crystal structure of **1** ($P2_1/c$, No. 14) with four molecules in a monoclinic unit cell has centrosymmetric C_{2h} symmetry, making phonons in either *g* (A_g, B_g) or *u* (A_u, B_u) modes. Transitions between ZFS states are primarily magnetic-dipole allowed,[30] making them *g*-*g* transitions in centrosymmetric C_{2h}.[25] However, when considering the local symmetry in C_{2v} for one molecule of **1** (with no inversion center at the Co^{II} ion), $M_S = \pm 3/2$ and $\pm 1/2$ states are represented by $E_{1/2}$ (or Γ_5) in C_{2v}' double group.[69-70]

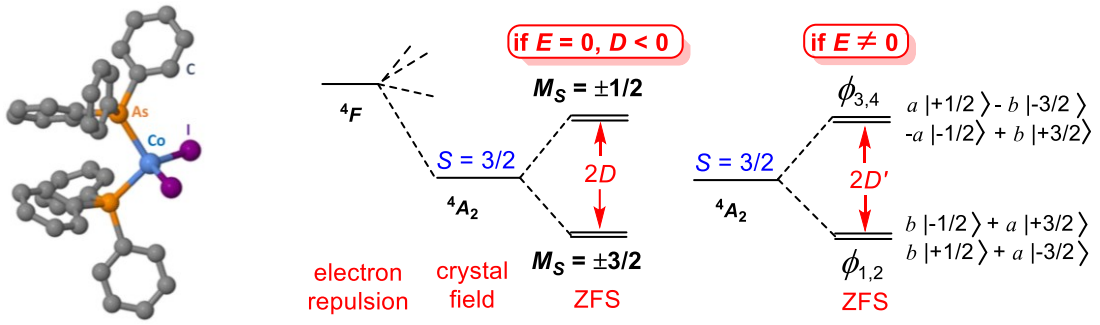

Figure 1. (Left) Structure of $Co(AsPh_3)_2I_2$ (**1**). (Middle) ZFS pattern of a high-spin Co^{II} ion with $D < 0$, $E = 0$. (Right) Quartet levels in **1** with lower symmetry [$E \neq 0$, $D' = (D^2 + 3E^2)^{1/2}$]; Mixing coefficients $a = \cos\beta$ and $b = \sin\beta$ are described by the mixing angle β [$\tan 2\beta = \sqrt{3}\,(E/D)$].[67-68]

FIRMS

Transmission spectra of **1** (Figure 2) reveal a weak magnetic transition originating at ~54 cm^{-1}, splitting linearly with field and revealing weak avoided crossings with IR-active phonons.[48] The couplings, not immediately recognizable in the raw spectra (Figure 2-Middle) but clear in the contour plots (Figure 2-Bottom), do not displace entire peaks, and instead only appear to involve a small portion of phonon intensities.

Reflectance spectra of an unoriented single crystal of **1** [Figure S1 in Supporting Information (SI)] show that, while the contour plot (Figure S1-Bottom) is not as clear as Figure 2-Bottom, avoided crossings are clearly seen at the strongest interaction points, i.e., points of the closest proximity. Figure S1-Top also shows extremely weak intensity shifting to lower energies with field (i.e., red-shift). We attribute blue- and red-shift peaks in both transmission and reflectance spectra to $M_S = -3/2$ (ϕ_1) $\rightarrow -1/2$ (ϕ_3) and $M_S = +3/2$ (ϕ_2) $\rightarrow +1/2$ (ϕ_4) transitions, respectively. Due to the low temperature of the sample (5.3 K), ground state (ϕ_1) is appreciably populated at applied fields by Boltzmann statistics. As the fields increase, relative energy of the ϕ_2 state increases, leading to further intensity decreases for transitions originating from this state.

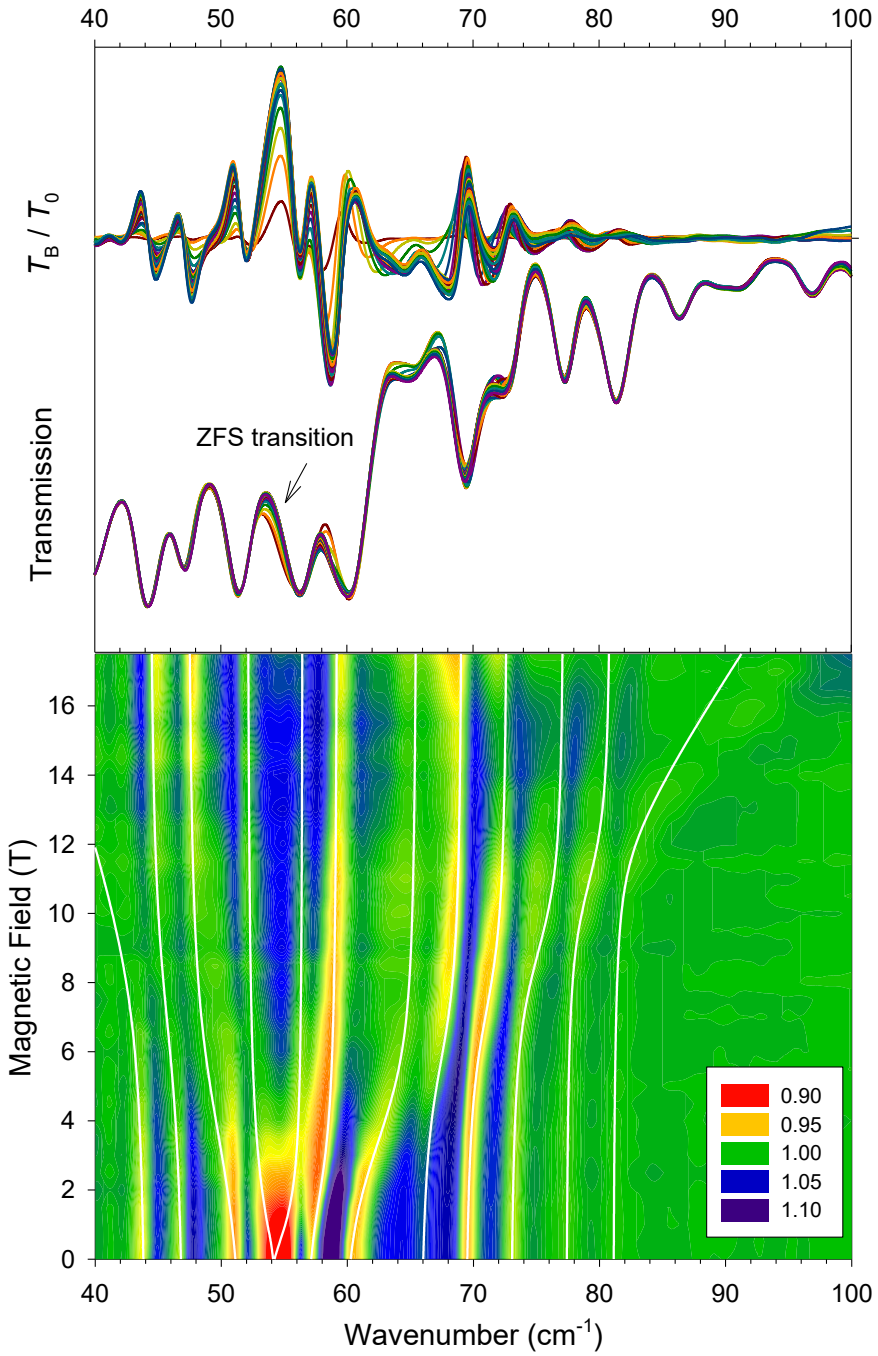

Figure 2. (Top) Spectra normalized to the zero-field spectrum. (Middle) Transmission FIRMS spectra of **1** at 5.3 K. The peaks pointing down are phonons. (Bottom) Contour plot of normalized data (by average across all fields). White lines indicate fittings from Eq. 2. Fitting parameters are shown in Table S1.

Compound **1** is part of a growing set of Co^{II}-based SMMs reported in recent years, displaying a magnetic peak clearly involved in avoided crossings with neighboring phonons.[23,25,48,55] These couplings can obscure the origin of the magnetic peak, making direct determination of the peak extremely difficult using only the FIRMS spectra. These couplings, displayed in a contour plot of the normalized spectra, can be visually fit using a spin-phonon coupling model to assist in determining the peak location at zero field.[25,48]

In the simplest phenomenological model not including potential field dependency, a single spin-phonon coupling can be fit using a Hamiltonian matrix in Eq. 1.[71] Eigenvalues of Eq. 1 at each field give energies of the coupled peaks, showing a repulsion instead of crossing without interacting.

$$H = \begin{pmatrix} E_{sp} & \Lambda \\ \Lambda & E_{ph} \end{pmatrix} \quad (1)$$

where E_{sp} and E_{ph} = energies of a magnetic/ZFS $|\Psi_{sp}\rangle$ and phonon $|\Psi_{ph}\rangle$ peak, respectively. Λ = coupling constant dictating the interaction between both peaks (Λ = half the distance in energy between them at their closest point of interaction).

Using an expanded matrix, e.g., Eq. 2, we have fit each of the avoided crossings simultaneously. This fitting assumes the blue-shifting peak couples with seven phonons while the red-shifting peak interacts with only three. It is possible they couple with additional phonons. However, for powder samples, the magnetic peaks tend to broaden and become weaker with higher fields due to crystal orientations, making additional couplings too weak to observe, even in the normalized contour plot.

$$H = \begin{pmatrix} E_{sp1} & 0 & \Lambda_1 & \Lambda_2 & \Lambda_3 & 0 & 0 & 0 & 0 & 0 & 0 & 0 \\ 0 & E_{sp2} & 0 & 0 & 0 & \Lambda_4 & \Lambda_5 & \Lambda_6 & \Lambda_7 & \Lambda_8 & \Lambda_9 & \Lambda_{10} \\ \Lambda_1 & 0 & E_{ph1} & 0 & 0 & 0 & 0 & 0 & 0 & 0 & 0 & 0 \\ \Lambda_2 & 0 & 0 & E_{ph2} & 0 & 0 & 0 & 0 & 0 & 0 & 0 & 0 \\ \Lambda_3 & 0 & 0 & 0 & E_{ph3} & 0 & 0 & 0 & 0 & 0 & 0 & 0 \\ 0 & \Lambda_4 & 0 & 0 & 0 & E_{ph4} & 0 & 0 & 0 & 0 & 0 & 0 \\ 0 & \Lambda_5 & 0 & 0 & 0 & 0 & E_{ph5} & 0 & 0 & 0 & 0 & 0 \\ 0 & \Lambda_6 & 0 & 0 & 0 & 0 & 0 & E_{ph6} & 0 & 0 & 0 & 0 \\ 0 & \Lambda_7 & 0 & 0 & 0 & 0 & 0 & 0 & E_{ph7} & 0 & 0 & 0 \\ 0 & \Lambda_8 & 0 & 0 & 0 & 0 & 0 & 0 & 0 & E_{ph8} & 0 & 0 \\ 0 & \Lambda_9 & 0 & 0 & 0 & 0 & 0 & 0 & 0 & 0 & E_{ph9} & 0 \\ 0 & \Lambda_{10} & 0 & 0 & 0 & 0 & 0 & 0 & 0 & 0 & 0 & E_{ph10} \end{pmatrix} \quad (2)$$

This fitting assumes that couplings between E_{sp1} and $E_{ph4\text{-}10}$ as well as between E_{sp2} and $E_{ph1\text{-}3}$ are nonexistent. In reality, the coupling is nonzero, but likely vanishingly small. The fitting results, , yielding coupling constants Λ = 1.5–2.1 cm^{-1} (Table S1).

Results of our fits are in a good agreement with experimental data with lines in Figures 2 and S1 following the shift of each peak. As the $\phi_1 \rightarrow \phi_3$ peak shifts to higher energies (Figure 2), it experiences an avoided crossing with each phonon until ~80 cm^{-1}. The red-shifting $\phi_2 \rightarrow \phi_4$ peak behaves similarly, with the exception that the magnetic peak eventually disappears below ~45 cm^{-1} at 7-9 T. In this fitting, the ZFS transition originates from 54 cm^{-1} and splits into two peaks residing at ~35 and ~90 cm^{-1} by 17 T.

RaMS

In the RaMS studies,[72] a single crystal was excited with a 532 nm laser with magnetic fields from 0 to 15 T. Results agree well with those of FIRMS, showing a ZFS peak originating at ~54 cm^{-1} shifting to 90 cm^{-1} by 14 T (Figure 3). This peak shifts linearly with magnetic fields, and does not noticeably broaden with fields. This is expected, since only a single

orientation/crystal face was measured. Unlike in FIRMS, the ZFS peak does not appear to couple to any phonons with the exception of a single phonon at 60 cm^{-1}. The coupling can be fit using Eq. 1, giving a relatively small $\Lambda = 1.0$ cm^{-1}.[71]

Due to the dense population of phonons, it is not clear whether the ZFS peak is Raman-allowed by its own intensity or if it must rely on the borrowed intensity of nearby phonons. This latter case includes RaMS of $Co(acac)_2(H_2O)_2$ showing no ZFS peak at zero-field.[25] Only when it shifts into close proximity to adjacent *g* phonons does the ZFS peak steal intensity from these phonons in avoided crossings. Once the ZFS peak passes the phonons, it gradually disappears again.[25] A similar phenomenon may happen here. The magnetic peak is easily observed at zero-field in the midst of several phonons. Once the ZFS peak is in regions with few phonons, such as 66-71 cm^{-1} and >77 cm^{-1}, it becomes exceedingly weak. It is worth noting the structural differences between $Co(AsPh_3)_2I_2$ (**1**) and $Co(acac)_2(H_2O)_2$,[25] which, to our knowledge, are the only two metal complexes displaying spin-phonon couplings in RaMS spectra. The molecular (or local) symmetry of $Co(acac)_2(H_2O)_2$ is C_{2h} with the Co(II) ion at the inversion center of both the molecule and the crystallographic unit cell.[25,73] In comparison, the inversion center in the unit cell of $Co(AsPh_3)_2I_2$ (**1**) is among four molecules, each with local C_{2v} symmetry.

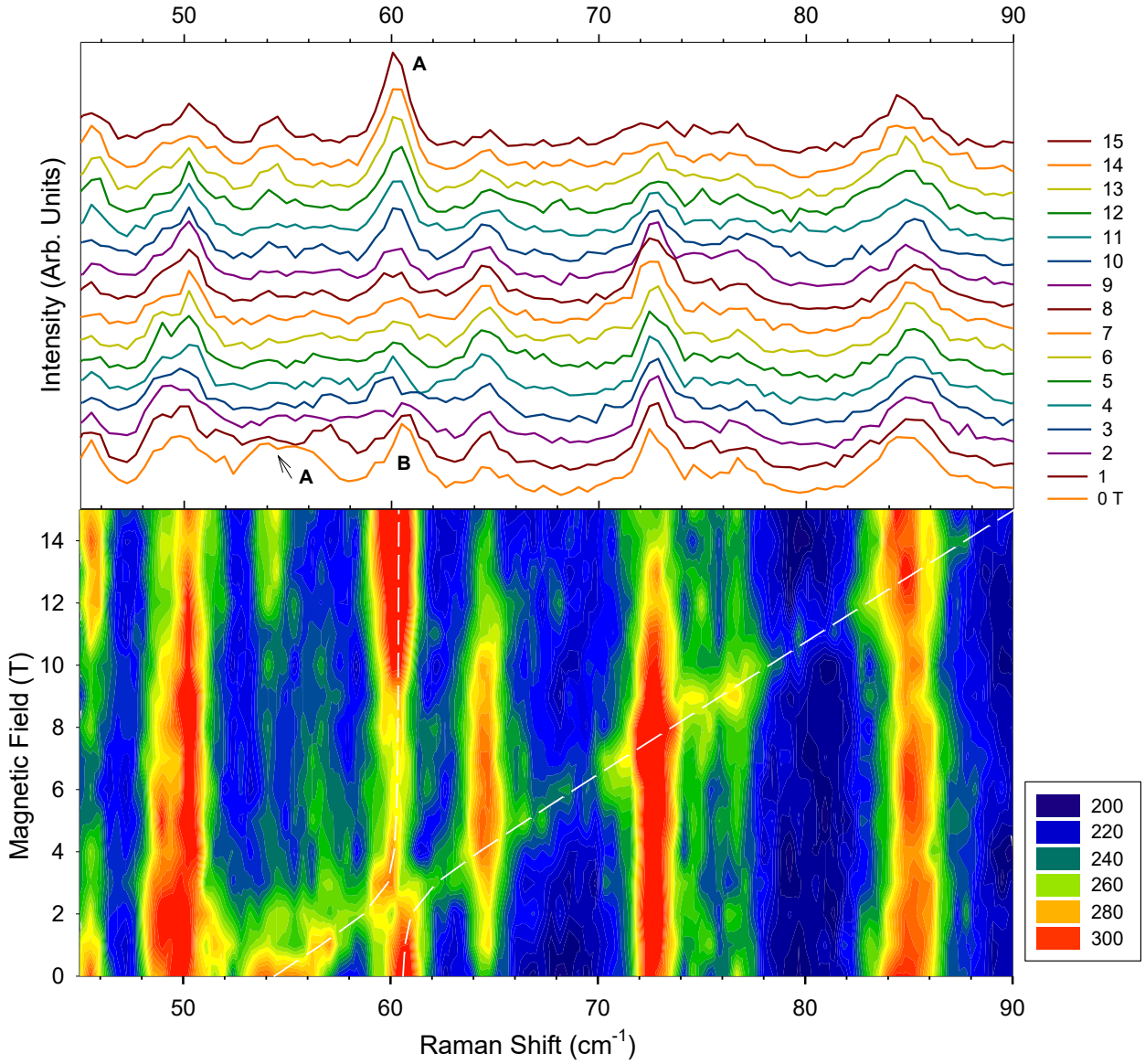

Figure 3. (Top) Stacked Raman spectra of **1** at 0-15 T and 5 K. Peak **A** = ZFS transition, **B** = phonon. After spin-phonon coupling (as an avoided crossing at 2-3 T), peak **A** has become a phonon at 14 T, while peak **B** has become magnetic and blue-shifted. (Bottom) Contour plot of RaMS for **1**. The white line indicates a fit of an avoided crossing with peak **B** using Eq. 1.

INS

INS studies of **1** were conducted at both indirect-geometry VISION[74] and direct-

geometry DCS[75] at 0, 5, and 10 T. Use of different INS instruments in coordination chemistry was recently reviewed.[42]

As magnetic peaks are stronger at low |***Q***| (known as forward scattering; ***Q*** = vector of momentum transfer) in VISION, forward scattering data were used. In INS spectra, phonons tend to attenuate with increased temperatures. This is mitigated by Bose-correction, making phonon intensities at different temperatures about the same in Bose-corrected spectra and thus easier to identify magnetic peaks. In Figure 4, the ZFS peak at ~53 cm^{-1} decreases in intensity significantly at 50 K and nearly disappear at 100 K, by the Boltzmann distribution of molecules to the excited KD $\phi_{3,4}$ (Figure 1), while phonons do not show such noticeable changes. We suspect that the ZFS peak of **1** is in a region with many phonons overwhelming the magnetic peak. To address this issue, INS of **1** at different magnetic fields at DCS were studied.

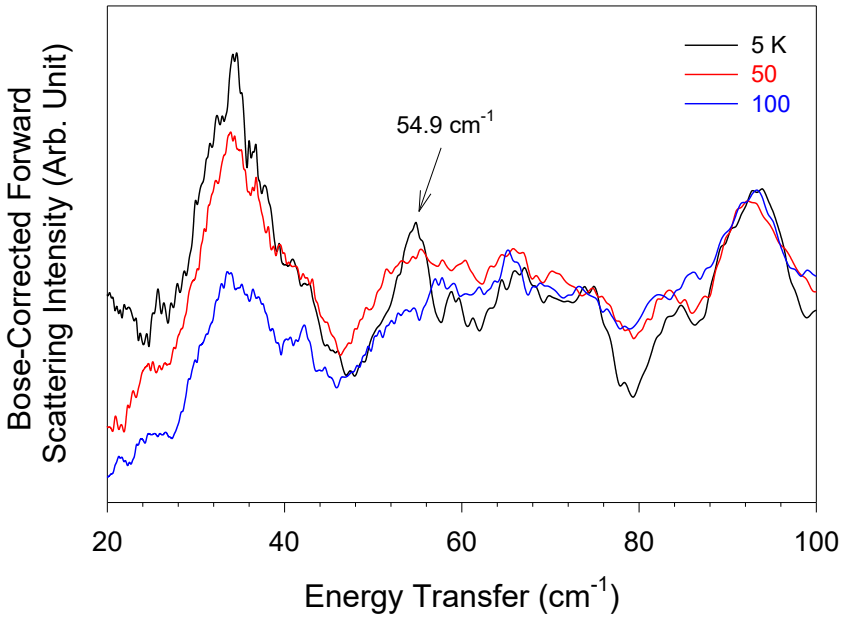

Figure 4. Forward-scattering INS spectra of powders of **1** at 5, 50, and 100 K at VISION.

Signal-to-noise ratios of the peaks in DCS spectra are low, as the magnet blocks many

detectors. Variable-field INS spectra of **1** at DCS (Figure 5) show a strong peak at 54.4 cm^{-1} overlapping with a phonon. With field increases, the Zeeman effect shifts the magnetic peak to higher energies, while phonons remain at the same position. At 5 T, the magnetic peak shows up at 61.6 cm^{-1} and the intensity of the peak at 53.2 cm^{-1} was reduced. At 10 T, the ZFS peak shifts further to 67.3 cm^{-1} and leaves a phonon peak at 61.5 cm^{-1}. The phonon peak at 35.6, 41.7 and 74.9 cm^{-1} remained at the same position with changing magnetic field. This peak shifting pattern indicates that the ZFS peak is located at 54.4 cm^{-1} at 0 T.

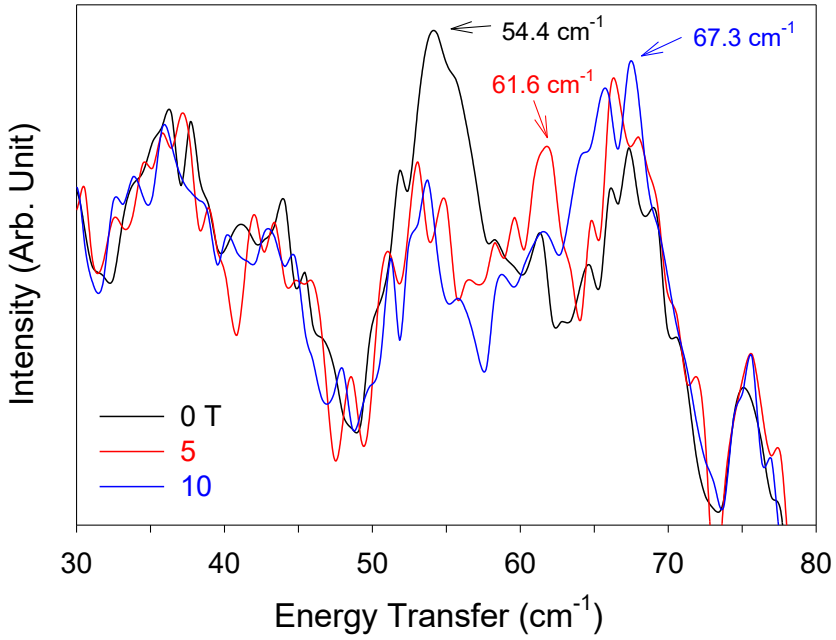

Figure 5. INS spectra of powders of **1** at 1.5 K under 0, 5 and 10 T magnetic fields at DCS.

Electronic Structure Calculations

To further elucidate the nature of ZFS, calculations using the complete active space self-consistent field (CASSCF) followed by N-electron valence perturbation theory (NEVPT2) were performed on the crystal structure of **1**. Energies of the spin-free quartet and doublets states are

provided in Table S3. As per the C_{2v} splitting pattern, the $^4T_2$ first excited state in T_d geometry splits into the $^4A_1$, $^4B_1$ and $^4B_2$ excited states and NEVPT2 computed energies of these states are ~2859 cm^{-1}, 3336 cm^{-1}, and 3905 cm^{-1}, respectively. According to the NEVPT2-computed SOC spectrum, the energy gap between the ground- and first-excited KD is 35.8 cm^{-1} (NEVPT2). Wavefunction decomposition analysis indicates the ground state $^4A_2$ KD composition to be 74%|3/2; ±3/2⟩ + 21% |3/2; ±1/2⟩. The calculated effective *g*-values for the ground state KD are g_{min} = 0.579, g_{mid} = 0.627, and g_{max} = 7.259, which are highly axial in nature (Figure S4). The projection of the quartet and doublet excited states of NEVPT2 (CASSCF) calculations onto an S = 3/2 pseudo-spin yields D = –17.9 (–20.5) cm^{-1} and E/D = 0.09 (0.17). The sign and magnitude of D and $|E/D|$ match nicely with experimental results. The small $|E/D|$ indicates highly effective axial behavior of the Co^{II} ion in **1**. Simulated magnetic susceptibility and magnetization data using computed spin-Hamiltonian (SH) parameters are in good agreement, reflecting the reliability of the computed SH parameters (Figure S4). The large ZFS of (–17.0) –20.7 cm^{-1} results from the local C_{2v} symmetry, allowing mixing of the ground and low-lying excited states via spin-orbit coupling. The largest contributions to ZFS arise from the three low-lying excited quartet states $^4A_1$, $^4B_1$, and $^4B_2$. The negative value of D stems from the mixing between the d_{x2-y2} and d_{xy} orbitals via the *z*-component of the orbital operator (Figure S5). A small contribution from the low-lying $^2T_2$ (^2G) doublet states is also computed, resulting from excitations within the t_2-subshell.

Ab initio ligand field theory (AILFT) allows one to extract ligand field parameters using CASSCF wavefunctions along with CASSCF energy eigenvalues and their second-order energy corrections for dynamical correlation (NEVPT2). These parameters are a 5 × 5 matrix of the effective one-electron ligand field and Racah parameters B and C describing spherically-

averaged interelectronic repulsions within the d^n shell of the transition metal, i.e., d^7 for **1**.

The NEVPT2 ligand field matrix (Eq. 3) yields, in a hidden way, valuable information about the metal-ligand interactions; unraveling this information is best done in the framework of the angular overlap model (AOM).[76] It allows for the presentation of the matrix elements

$$V(NEVPT2) = \begin{bmatrix} 1187 & -48 & -65 & 19 & 1252 \\ -48 & -1488 & -94 & -251 & 50 \\ -65 & -94 & 1794 & 31 & 562 \\ 19 & -251 & 31 & 331 & -113 \\ 1252 & 50 & 562 & -113 & -1824 \end{bmatrix} \quad (3)$$

of the effective ligand field Hamiltonian $V_{ij} = \langle d_i \,|\hat{V}_{eff}|\, d_j \rangle$ as a sum of terms from each of the ligands, I^- and $AsPh_3$ (Eq. 4).

$$V_{ij} = a_{ij}^{\sigma_i}\sigma_I + a_{ij}^{\pi_i}\pi_I + a_{ij}^{\sigma_{\mathrm{As}}}\pi_{\mathrm{As}} \quad (4)$$

Each of these contributions is factorized by a factor $a_{ij}^{\lambda_L}$ depending on the ligand (L) position which is the function of geometric angles extracted from the X-ray structure of the complex, times parameters characterizing each interaction of the metal with the ligand. These parameters are "standardized" using metal 3d type atomic orbitals (AOs) and ligand AOs ideally aligned for σ and π interactions. These parameters do not depend on the complex geometry but only on the metal-ligand distance and the given ligand's nature. In **1**, I^- is expected as a σ- and π-donor, while $AsPh_3$ is solely a σ-donor, as the π-orbitals on the As atom is involved in strong bonds to the three phenyl groups. These parameters are defined in Figure 6 as the destabilization of the metal 3d-orbital by covalent antibonding and electrostatic interactions with I^- and $AsPh_3$,

which can hardly be separated in $\sigma_{\mathrm{I}}, \pi_{\mathrm{I}}, \sigma_{\mathrm{As}}$.

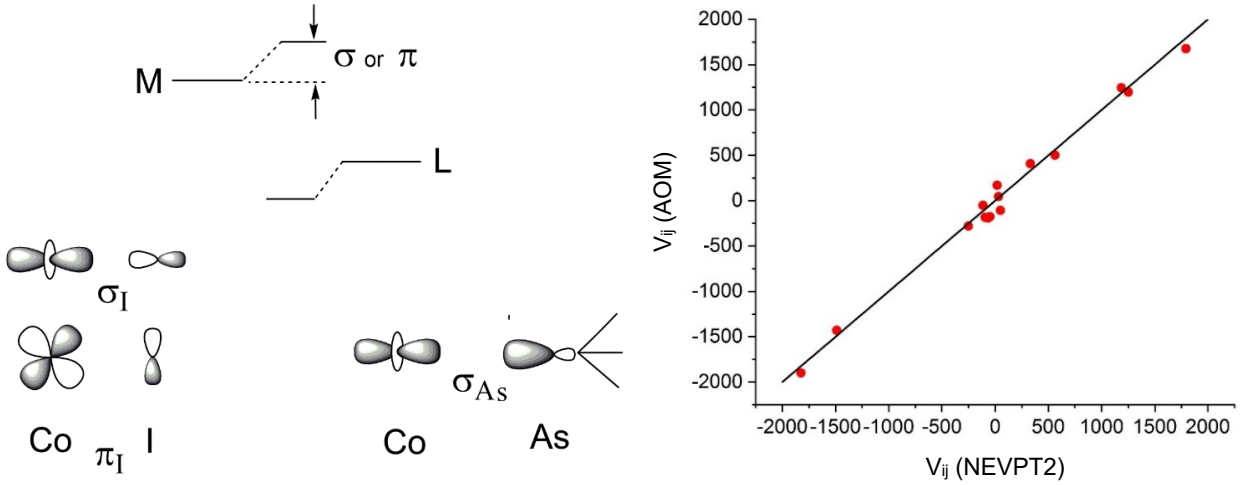

Figure 6. (Left) Definition of the angular overlap model parameters for Co-I (σ_{I} and π_{I}) and Co-As (σ_{As}) along with the corresponding energy destabilization effect of the Co $d_{\sigma}(d_{z^2})$ and $d_{\pi}(d_{xz,yz})$. (Right) NEVPT2 matrix elements (abscissa) and their values computed using Eq. 4 along with values of a best fit of the parameters $\sigma_{\mathrm{I}}, \pi_{\mathrm{I}}, \sigma_{\mathrm{As}}$ (see Table 1).

A best fit of the parameters $\sigma_{\mathrm{I}}, \pi_{\mathrm{I}}, \sigma_{\mathrm{As}}$ using the values of the matrix elements in Eq. 3 results in numerical values (Table 1) reproducing the NEVPT2 matrix elements with remarkable consistency (Figure 6). The results allow one to characterize I^- as a weak σ- and π-donor, while $AsPh_3$, based on the consistency of the adopted bonding model, as pure σ-donor. While σ_{I} and σ_{As} are *slightly* larger for NEVPT2 than the CASSCF results, values of π_{I} from the two treatments are almost the same. As shown earlier,[77] this effect is due to the constrained form of NEVPT2 Hamiltonian incorporating the dynamic correlations only at the level of total energies, as the wavefunction is at the CASSCF level only. As a result of this constraint, the CASSCF and NEVPT2 results are quite close in values and induce substantial standard deviations in the latter

AILFT method. Thus, going from CASSCF to NEVPT2 does not reflect the expected increase of covalency, which should be quite large for both ligands. For this reason, we also derived values for σ_{I}, π_{I}, and σ_{As} (Table 1) using a direct fit to energies of spin-allowed d-d transitions, as in spectroscopy. On comparison, dynamical correlation induces a considerable increase of σ_{I}, π_{I}, and σ_{As} from the CASSCF to the NEVPT2 results.

Table 1. Values of the angular overlap model parameters $\sigma_{\mathrm{I}}, \pi_{\mathrm{I}}, \sigma_{\mathrm{As}}$ (cm^{-1}) from AILFT and from a direct fit to spin-allowed d-d transition.

Parameters	AILFT		Direct fit to energies of spin (S = 3/2) allowed d-d transitions	
	CASSCF	NEVPT2	CASSCF	NEVPT2
σ_{I}	2666	2831	1188	1884
π_{I}	1368	1387	2355	3843
σ_{As}	2932	3148	2548	3876
Standard deviation V_{ij} (NEVPT2) - V_{ij} (AOM)	90	98	102	170

It is interesting to compare the electronic structures of **1** with analogous $Co(PPh_3)_2I_2$ which was characterized experimentally in Ref. 32. The polarized d-d absorption spectrum of the $Co(PPh_3)_2I_2$ reported by Tomlinson et al.[78] allowed identifications of six spin-allowed d-d transitions to afford deducing ligand field parameters from a best fit to these transitions: $\sigma_I = 2177$; $\pi_I = 633$; $\sigma_P = 2502$; $\pi_P = -1482$ (cm^{-1}) claiming that the phosphor donor acts as a π-acceptor, which was also proposed earlier by Davies et al.[79] To check this proposal, we have carried out CASSCF/NEVPT2 calculations using the X-ray crystal structure of $Co(PPh_3)_2I_2$,[17]

giving angular overlap parameters (Table 2) to compare with those of **1**. We have allowed for non-zero values of π_X parameters of X = As and P ligands. This might be due to low-lying empty 5d(4d) orbitals of As(P) which are in principle able to accommodate 3d electrons from the more than half filled d^7 Co(II) configuration. Since the sp^3 character of these ligands lacks π-electrons for bonding, these parameters were fixed at zero in Table 1. The AILFT results in Table 2 are not in support of πX acidities of the As and P ligands; π_X are, as expected, close to zero. However, based on our ab-initio calculations of Co-X (X = As, P), π -back bonding cannot be ruled out with underlying reasons in SI.

Table 2. Values of the angular overlap model parameters (cm^{-1}) σ_I , π_I ; σ_X and π_X (X = As, P) from a best fit to the corresponding 5 × 5 AILFT ligand field matrices from CASSCF/NEVPT2 calculations using X-ray structures from Ref. 17.

	X = As		X = P	
σ_I	2832	2775	2788	2825
π_I	1385	1345	1356	1384
σ_X	3147	3180	3736	3716
π_X	-	-96	-	58
Standard Deviation	98	97	112	111

Phonon Calculations and Comparison with Spectra

While VISION spectra (Figure 4) illuminate the magnetic peak through variable-temperatures alone, it is often difficult to do so without other spectra to compare to. We have calculated the INS phonon spectrum using periodic DFT calculations in VASP (Vienna Ab initio Simulation Package).[17] The crystallographic symmetry of $P2_1/c$ was used to assign phonon symmetries using the Phonopy program.[80] The calculated spectrum ≤300 cm^{-1} is shown in Figure 7 and compared with those from spectroscopies. Calculated phonons are listed in Table S2 in SI.

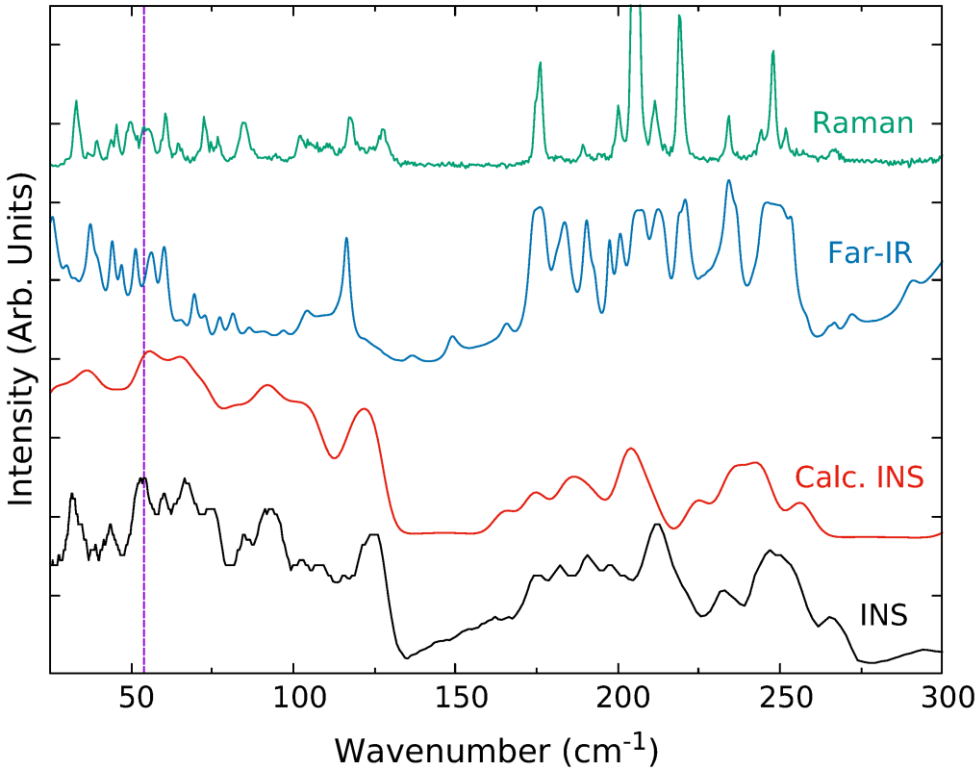

Figure 7. The 25-300 cm^{-1} region of experimental Raman, far-IR and backscattering INS (VISION) at zero field and 5.0 K with the calculated INS spectrum. The vertical line indicates the position of the ZFS peak at 54 cm^{-1}. Far-IR approaches zero transmittance above 300 cm^{-1} due to the amount of sample present. Raman at 300-550 cm^{-1} and experimental and calculated INS spectra at 300-4000 cm^{-1} are given Figure S2.

Comparison of the calculated and experimental INS spectra shows a reasonable match throughout the entire range, even though many peaks do not line up exactly. Below ~150 cm^{-1}, the calculation does not accurately simulate the finer structure, only fitting to the general shape of the spectrum, as the low-energy region is notoriously difficult to calculate. As a result, these calculations are not useful for comparison with the VISION spectrum to determine the location of the ZFS peak, but do provide insight into many of the phonon motions for each calculated mode. Due to the lack of symmetry selection rules in INS, all calculated phonons within the entire Brillouin zone in the calculated spectrum are expected. In contrast, both far-IR and Raman are limited by symmetry selection rules and can only view modes originating at the Γ-point in the Brillouin zone. Nevertheless, each method provides a unique look at the phonon and magnetic modes of **1**.

Comparison between the Various Methods for the Extraction of Spin-Hamiltonian Parameters

Magnetic sublevels of the $S = 3/2$ ground state, two Kramers doublets (KDs) and their splitting in a magnetic field, are described by the spin-Hamiltonian in Eq. 5:

$$\hat{H}_{sh} = D(\hat{S}_z^2 - S(S+1)/3) + E(\hat{S}_x^2 - \hat{S}_y^2) + \mu_B(g_x B_x \hat{S}_x + g_y B_y \hat{S}_y + g_z B_z S_z) \quad (5)$$

D and E = axial and orthorhombic ZFS parameters; g_x, g_y, g_z = g factors. This equation is in the canonical magnetic frame in which the ZFS tensor becomes diagonal with D_{xx}, D_{yy}, D_{zz} parameters so the $\boldsymbol{D}$ tensor is traceless ($D_{xx} + D_{yy} + D_{zz} = 0$). D and E are defined by Eqs. 6 and 7:[81]

$$D = (3/2)D_{zz} \quad (6)$$

$$E = (1/2)(D_{xx} - D_{yy}) \quad (7)$$

ZFS, energy splitting of the two KDs, is given by the expression $E_{sp} = 2\sqrt{D^2 + 3E^2}$ and has been extracted from VT-INS, FIRMS and RaMS, giving E_{sp} = 54 cm^{-1}. The most impressive result is the ability of the different spectroscopies to yield E_{sp}., the same value coinciding almost perfectly with that (51 cm^{-1}) from CASSCF computations.

Assuming no orthorhombicity (E = 0), D = 1/2 E_{sp}, giving the values in Table 3. Magnetometry did not give the accurate D value, illustrating that the bulk, non-resonant technique may not yield reliable ZFS parameters. Surprisingly NEVPT2 slightly underestimates D. Contrary to spectroscopies, theoretical calculations yield all spin-Hamiltonian parameters. The calculations show that roughly, E can be neglected [E(CASSCF) = 0.5 cm^{-1}, E(CASSCF/NEVPT2) = 1.6 cm^{-1}, D(CASSCF) = -25.70 cm^{-1}, D(NEVPT2) = -17.90 cm^{-1}].

Comparisons of Experimental Techniques to Probe Magnetism of Transition Metal Complexes

Several advanced spectroscopies have been used in the current work. Their features and those of a few other techniques we have employed in other studies are listed in Table 4 for comparison. Krzystek and Telser have reviewed experimental techniques, including magnetometry, EPR (including HFEPR), frequency-domain magnetic resonance (FDMR), INS, magnetic circular dichroism (MCD), and Mössbauer spectroscopy, to measure large magnetic anisotropy in transition metal complexes.[4] Baker and coworkers have also discussed spectroscopic methods to study molecular nanomagnets.[53] FDMR can measure energies to 48 cm^{-1}.[4,82] However, it has mostly fallen out of use, as some parts are no longer manufactured.

Table 3. Spin-Hamiltonian parameters for **1** (Eq. 5) from spectra, magnetometry, and CASSCF and NEVPT2 calculations.[a]

Method	$E_{sp} = 2\sqrt{D^2 + 3E^2}$	D[b]	E/D	g_x	g_x'		g_y	g_y'		g_z	g_z'		Ref.
					KD1	KD2		KD1	KD2		KD1	KD2	
VT-INS	54.9	-27.45	-	-			-			-			This work
FIRMS	54.0	-27.00	-	-			-			-			This work
RaMS	54.0	-27.00	-	-			-			-			This work
Magnetometry	149.4	-74.7	-	-			-			-			Ref. 17
CASSCF	51.43	-25.7	0.02	2.400	0.186	4.930	2.362	0.106	4.640	2.654	7.961	2.646	This work
CASSCF/NEVPT2	36.91	-17.9	0.09	2.278	0.576	3.917	2.234	0.627	5.053	2.440	7.262	2.381	This work

[a] g_x', g_y', g_z' = Effective g-factors in an $s' = 1/2$ pseudo-spin Hamiltonian for ground KD1 and excited KD2.

[b] Values of D assuming $E/D = 0.0$.

Table 4. Experimental techniques to probe magnetism of transition metal complexes[a,b]

Technique	Parameter(s) of Interest	Approx. Energy Range (cm^{-1})	Features
Far-IR magneto-spectroscopy (FIRMS)[23,25,27]	• D' for Kramers ions • D, E for non-Kramer ions	Typically, 12-720 cm^{-1} [c]	• Revealing magnetic transitions, i.e., energies of magnetic excited levels for complexes with either unquenched or quenched orbital angular momenta. • For complexes with zero-field splitting (ZFS) (i.e., quenched orbital angular momenta), direct and precise determination of D' or D, E • Broad spectral range. • Revealing spin-phonon couplings with IR-active phonons[d] (such as *u* phonons in centrosymmetric crystals). • Appearance of phonons near the magnetic peak potentially complicating direct observation of the latter due to spin-phonon coupling. • Small amount of powder samples (≤5 mg) or single crystals; Samples typically disposed after use. • Resolution at 0.3 cm^{-1} for the facilities at NHMFL.[b,83] • Single temperature of ~5.5 K for the facilities at NHMFL.[83]
Raman magneto-spectroscopy (RaMS)[25]	$\|D'\|$ g_x, g_y, g_z	10-3000 cm^{-1} (direct optic probe) 70-3000 cm^{-1} (fiber optic probe) based on the facilities at NHMFL[72]	• Relatively broad energy range. • Revealing spin-phonon couplings with Raman-active phonons (such as *g*-phonons in centrosymmetric crystals). • A small crystal required, although powder samples may be used. • Appearance of phonons near the magnetic peak potentially complicating direct observation of the latter. • Selection rules for ZFS transitions in Raman spectroscopy not well understood. • Limited instrumental availability, requiring Raman filters and optical systems to observe low energy peaks. • Resolution at 1-2 cm^{-1} for the facilities at NHMFL.[72]
Inelastic neutron scattering (INS)[42,53]	$\|D'\|$	10-8000 cm^{-1}	• Revealing magnetic transitions, i.e., energies of magnetic excited levels for complexes with either unquenched or quenched orbital angular momenta. • For complexes with ZFS, direct determination of $\|D'\|$; Sign of D when M_S = 5/2 and 2^{51} by an direct-geometry INS spectroscometer[42] such as CNCS[84] at ORNL[b] or DCS[75] at NCNR.[b] • Broad energy range for indirect-geometry spectroscometer[85] such as VISION[74] at ORNL. • Distinguishing between magnetic and phonon transitions via temperature-,[32]

			field-,[48] and/or $\|\boldsymbol{Q}\|$[e]-dependences,[51] depending on whether the spectrometer is direct- or indirect-geometry. • Truly zero-field techniques requiring no magnet, although a magnet may be used to reveal additional properties; The magnet often blocks large portions of neutron detectors, leading to longer data acquisition and increased background. • No symmetry-based selection rule for phonons, leading to the observation of all phonon peaks. • Resolutions varied depending on the energy ranges.[74,84] • DFT-calculated phonon INS spectra by, e.g., VASP program for comparison with experimental INS spectra, helping identify magnetic peaks.[32] • Limited instrumental availability. • Large amount of powder samples (typically ≥0.5 g). • Samples *possibly* becoming radioactive, requiring decay times before reuse.
High-field, high-frequency EPR (HFEPR)[86]	D, E, g_x, g_y, g_z	Typically <33 cm^{-1}	• Highly accurate, direct determination of D and E parameters and g tensors. • Only magnetic-dipole-allowed transitions observed; However, phonons may give complex spectra through spin-phonon couplings. • When $D < 0$, $E = 0$ (with no mixing of states, e.g., shown in Figure 1), the transition within the ground doublet ($-M_S \rightarrow +M_S$) is forbidden.[f,71] • Compatible with Kramers and non-Kramers complexes depending on accessible frequencies and fields. • Limited energy range: ZFS transitions up to 30 cm^{-1} in non-Kramers (S = integers) and 15 cm^{-1} in Kramers complexes for the user facilities at NHFML • Limited instrumental availability. • ZFS indirectly determined by multi-parameter fits to the field/frequency dependencies of the resonances. • Small amount of powder samples (≤100 mg) or single crystals. • Powder samples may be reused.
Conventional EPR (X- and Q-band)[87-88]	D, E, g_x, g_y, g_z	<0.3 cm^{-1} (X-band) or 1.2 cm^{-1} (Q-band)	• Widely available instrumentation compared to HFEPR. • Limited energy range. • Typically incompatible with non-Kramers or easy-axis Kramers ions (i.e., $D < 0$, $E = 0$) due to frequency and field limitations (such systems are called *EPR-silent*). • Small amount of powder samples (≤100 mg) or single crystals. • Powder samples or single crystals which may be reused.
Magnetometry	**DC:**[g]		• Suitable for a variety of compounds with no limits of ZFS

(Magnetic susceptibility measurement)[2,4,89]	*D*, *E*, *g*, *C*, θ, μ_{eff}, M_s, M_r, H_c, T_C, T_N **AC:**[h] τ, Relaxation mechanisms including the direct, Raman, and Orbach processes, U_{eff}		• Bulk, non-resonant technique likely prone to error; Impurities may also contribute to the data, while spectroscopies may detect the impurities and samples individually • Indirect determination of ZFS parameters • Challenging to measure accurately compounds with small magnetic moments • Difficult to distinguish the sign of *D* • Small amount of powder samples (≤100 mg) or single crystals • Sensitive to precise determination of sample mass and background correction from the sample holder • Samples reusable for other studies • Widely available instrumentation

[a] *D* and *E* = Axial and rhombic anisotropic parameters, respectively; $|D'| = (D^2 + 3E^2)^{1/2}$; *g* = Lande factor (or *g*-factor); g_x, g_y, g_z (also labled g_{xx}, g_{y-y}, g_{zz}) = Components in the $\boldsymbol{g}$ tensor.

[b] NHMFL = National High Magnetic Field Laboratory; ORNL = Oak Ridge National Laboratory; NCNR = NIST Center for Neutron Research.

[c] The instrument is also available in the IR range up to 6000 cm^{-1}.

[d] Phonons include vibrations of both molecules and crystal lattice.

[e] $\boldsymbol{Q}$ = Vector of momentum transfer in neutron scattering processes.[42]

[f] ΔM_S = 2, 3, 4, and 5 for transitions within the ground doublet in *S* = 1, 3/2, 2, and 5/2 complexes, respectively, while the selection rules for magnetic-dipole-allowed transitions are $\Delta M_S = 0, \pm 1$.[71] In fact, when *E* is small, leading to little mixing of the states, e.g., shown in Figure 1, it may still be difficult to observe the transitions within the ground doublet.

[g] *C* = Curie constant, θ = Weiss constant, μ_{eff} = Effective moment, M_s' = Saturation magnetization, M_r = Remnant magnetization, H_c = Coercive field, T_C = Curie temperature, T_N = Neel temperature.

[h] τ = Relaxation time, U_{eff} = Effective energy barrier for spin reversal in the Orbach processes.

Conclusions

Comprehensive spectroscopic studies of the magnetic and phonon features of **1** are presented. FIRMS, RaMS and INS all accurately determine the magnitude of the ZFS peak. Electronic calculations reveal the nature of the large magnitude and negative sign of ZFS, in reasonable agreement with experiments. Both FIRMS and RaMS show avoided crossings with nearby phonon peaks. Currently, it is unknown why the magnetic peak interacts mostly with IR-active modes and not Raman. These couplings may be present in INS, but we lack significant fields and energy resolution to distinguish them. Further research must be performed to determine the "selection rules" for spin-phonon couplings, as these modes likely hinder the performance of slow magnetic relaxation in high-temperature SMMs.

Experimental Section

Synthesis of 1. Complex **1** was synthesized and crystallized under N_2 using Schlenk techniques according to previously reported methods.[17] The compound is slightly air-sensitive.

FIRMS and RaMS. FIRMS and RaMS were conducted at NHMFL, Florida State University.

For FIRMS, the powdered samples were mixed with *n*-eicosane and pressed into pellets ~1 mm thick. Spectra were collected at 5.3 K using a Bruker Vertex 80v FT-IR spectrometer coupled with a superconducting magnet (SCM) with fields up to 17 T.

For RaMS, single crystals of **1** were mounted on a brass sample stage. Data were collected by a backscattering Faraday geometry using a 532 nm free-beam laser in a 14 T SCM cooled to 5 K in the Electron Magnetic Resonance (EMR) facility. Collected scattered light was guided via an optical fiber to a spectrometer equipped with a liquid nitrogen-cooled CCD camera.

INS with Variable Fields and Temperatures. Variable-field data were collected at the time-of-flight (TOF) DCS[75,90] on a 2.3 g of **1** wrapped with aluminum foil inside an aluminum can and placed in a 10 T vertical magnet and a dilution refrigerator. Data were collected up to 145 cm^{-1} at 1.5 K with an incident wavelength of 1.81 Å (201.6 cm^{-1}) at 0, 5, and 10 T. In addition, zero-field data at 20 K were collected, but no significant difference between the spectra at 1.5 and 20 K (0 T) was observed. Data processing was completed with Data Analysis and Visualization Environment (DAVE).[40] The INS experiments are particularly challenging, as the distance between the split magnet coils necessitates a smaller neutron beam, leading to reduction of the incident beam size by a factor of 2.5 and a concomitant shadowing of detectors, giving ~33% detector efficiency.

VT INS spectra at VISION,[74,91] Spallation Neutron Source (SNS), ORNL, were measured at 5, 25, 50, 75, and 100 K for 1 h at each temperature using the same 2.3-g sample of **1** in an aluminum container. VISION[91] provides data up to 4000 cm^{-1}. The inverted geometry design at VISION offers two banks of detectors for both forward (low $|\boldsymbol{Q}|$) and back (high $|\boldsymbol{Q}|$) scattering of neutrons. The phonon population effect was corrected by normalizing the INS intensity at energy transfer ω with $\coth\left(\frac{\hbar\omega}{2k_BT}\right)$.[40]

Electronic Structure Calculations. All electronic structure calculations were performed on the X-ray crystal structure data using ORCA 4.2.1 code.[92-93] We have employed a complete-active space self-consistent field (CASSCF)[94] with a minimal active space comprised of seven d-electrons in five active d-orbitals, i.e., CAS(7,5) for complex **1**. Scalar relativistic effects were incorporated employing the Doughlas-Kroll-Hess (DKH) approximation.[95] Here, we have employed the DKH-adapted version of the def2-TZVP basis set for Co, As, C, and H atoms.[96-97] DKH-adapted version of the Sapporo basis sets were employed for I atoms.[98] N-electron valence

perturbation theory (NEVPT2) calculations[99-101] were performed to capture the dynamic correlations. As an initial guess to the CASSCF calculations, we have used quasi-restricted orbitals (QROs) from DFT calculations. All 10 quartet and 40 doublet states were computed at both CASSCF and NEVPT2 levels of theory. AILFT analyses were performed to analyze the d-orbital ligand field splitting pattern.[102-104] To further quantify the nature of Co-As and Co-I bonds, 5 × 5 one electron ligand field matrix were fitted with e_σ and e_π parameters as defined in the Angular Overlap Model (AOM).

VASP[105] Calculations of 1. Geometry optimizations were performed based upon the single-crystal X-ray structure of **1** determined at 293 K. The optimized structure was used for the phonon calculations. Spin-polarized, periodic DFT calculations were performed using VASP with the Projector Augmented Wave (PAW)[106-107] method and the local density approximation (GGA)[108] + U (U = 5.0)[40] exchange correlation functional. The energy cut off was 800 eV for the plane-wave basis of the valence electrons. Total energy tolerance for electronic structure minimization was 10^{-8} eV. The optB86b-vdW non-local correlation functional that approximately accounts for dispersion interactions was applied.[109] For the structure relaxation, a 2 × 2 × 4 Monkhorst-Pack mesh was applied. Phonopy,[110] an open source phonon analyzer, was used to create the 1 × 1 × 1 supercell structure and extract symmetries. VASP was then employed to calculate the force constants on the supercell in real space using DFT.

Supporting Information

The Supporting Information is available free of charge at https://pubs.acs.org.

Author contributions, reflectance FIRMS spectra, table of fitting parameters of spin-phonon couplings in FIRMS transmission spectra, additional RaMS, INS and calculated INS

spectra, table of calculated INS phonons, additional results of the electronic calculations, and input file for ORCA calculations. Movies of phonons (vibrations) are also included.

Corresponding Authors

Mihail Atanasov - *Max Planck Institute for Coal Research, Kaiser-Wilhelm-Platz 1, D-45470 Mülheim an der Ruhr, Germany and Institute of General and Inorganic Chemistry, Bulgarian Academy of Sciences, 1113 Sofia, Bulgaria*; https://orcid.org/0000-0003-4178-2187; Email: mihail.atanasov@kofo.mpg.de

Zi-Ling Xue - *Department of Chemistry, University of Tennessee, Knoxville, Tennessee 37996, United States*; https://orcid.org/0000-0001-7401-9933; Email: xue@utk.edu

Notes

The authors declare no competing financial interest.

Acknowledgments

US National Science Foundation (NSF; CHE-1900296 and CHE-2055499 to Z.-L.X.; DMR-2004732 to S.H.) and a Shull Wollan Center Graduate Research Fellowship (Z.L. and S.E.S.) are acknowledged for partial support of the research. K.T. thanks a US Department of Navy HBCU/MI grant for support. K.R.D. gratefully acknowledges the National Science Foundation (CHE-1808779). Part of this work was performed at the National High Magnetic Field Laboratory which is supported by NSF Cooperative Agreement No. DMR-1644779 and the State of Florida. We acknowledge the support of the National Institute of Standards and Technology, U.S. Department of Commerce, in providing the Disk Chopper Spectrometer (DCS)

used in this work. Additional neutron scattering experiments were conducted at the VISION beamline at ORNL′s Spallation Neutron Source, which is supported by the Scientific User Facilities Division, Office of Basic Energy Sciences (BES), U.S. Department of Energy (DOE), under Contract No. DEAC0500OR22725 with UT Battelle, LLC. The computing resources were made available through the VirtuES and the ICEMAN projects, funded by the Laboratory Directed Research and Development program and the Compute and Data Environment for Science (CADES) facility at ORNL. We thank Dr. Wei Zhou of the NIST Center for Neutron Research (NCNR) for help with the DCS experiment. S.K.S. thanks IIT Hyderabad and DST (SRG/2020/001323) for the startup research grant.

References

1. Benelli, C.; Gatteschi, D., Single Ion Magnet (SIM). In *Introduction to Molecular Magnetism*, Wiley-VCH: 2015; pp 217-237. http://doi.org/10.1002/9783527690541.ch13
2. Frost, J. M.; Harriman, K. L. M.; Murugesu, M., The Rise of 3-*d* Single-Ion Magnets in Molecular Magnetism: Towards Materials from Molecules? *Chem. Sci.* **2016,** *7*, 2470-2491. http://doi.org/10.1039/C5SC03224E
3. Layfield, R. A., Organometallic Single-Molecule Magnets. *Organometallics* **2014,** *33*, 1084-1099. http://doi.org/10.1021/om401107f
4. Krzystek, J.; Telser, J., Measuring Giant Anisotropy in Paramagnetic Transition Metal Complexes with Relevance to Single-Ion Magnetism. *Dalton Trans.* **2016,** *45*, 16751-16763. http://doi.org/10.1039/C6DT01754A
5. McInnes, E. J. L.; Winpenny, R. E. P., Molecular Magnets. In *Comprehensive Inorganic Chemistry II*, Poeppelmeier, K., Ed. Elsevier: Amsterdam, 2013; pp 371-395. https://doi.org/10.1016/B978-0-08-097774-4.00419-8
6. Neese, F.; Pantazis, D. A., What is not Required to make a Single Molecule Magnet. *Faraday Discuss.* **2011,** *148*, 229-238. http://doi.org/10.1039/C005256F
7. Gao, S., *Molecular Nanomagnets and Related Phenomena*. Mingos, D. M. P., Structure and Bonding: 2015; Springer. https://link.springer.com/book/10.1007/978-3-662-45723-8
8. Chilton, N. F., Molecular Magnetism. *Annual Review of Materials Research* **2022,** *52*, 79-101. http://doi.org/10.1146/annurev-matsci-081420-042553
9. Gu, L.; Wu, R., Origins of Slow Magnetic Relaxation in Single-Molecule Magnets. *Phys. Rev. Lett.* **2020,** *125*, 117203. http://doi.org/10.1103/PhysRevLett.125.117203

10. Coronado, E., Molecular magnetism: from chemical design to spin control in molecules, materials and devices. *Nat. Rev. Mater.* **2020,** *5*, 87-104. https://doi.org/10.1038/s41578-019-0146-8

11. Zabala-Lekuona, A.; Seco, J. M.; Colacio, E., Single-Molecule Magnets: From Mn12-ac to dysprosium metallocenes, a travel in time. *Coord. Chem. Rev.* **2021,** *441*, 213984. https://doi.org/10.1016/j.ccr.2021.213984

12. Feng, M.; Tong, M.-L., Single Ion Magnets from 3d to 5f: Developments and Strategies. *Chem. Eur. J.* **2018,** *24*, 7574-7594. https://doi.org/10.1002/chem.201705761

13. Taylor, W. V.; Cashman, B. K.; Xie, Z.-L.; Ngo, K. K.; Rose, M. J., Synthesis and Magnetic Properties of Antimony-Ligated Co(II) Complexes: Stibines versus Phosphines. *Inorg. Chem.* **2022,** *61*, 6733-6741. https://doi.org/10.1021/acs.inorgchem.1c03366

14. Gatteschi, D.; Sessoli, R., Quantum Tunneling of Magnetization and Related Phenomena in Molecular Materials. *Angew. Chem. Int. Ed.* **2003,** *42*, 268-297. http://doi.org/10.1002/anie.200390099

15. Dey, M.; Gogoi, N., Geometry-Mediated Enhancement of Single-Ion Anisotropy: A Route to Single-Molecule Magnets with a High Blocking Temperature. *Angew. Chem. Int. Ed.* **2013,** *52*, 12780-12782. https://doi.org/10.1002/anie.201304982

16. Boča, R., Zero-Field Splitting in Metal Complexes. *Coord. Chem. Rev.* **2004,** *248*, 757-815. http://doi.org/10.1016/j.ccr.2004.03.001

17. Saber, M. R.; Dunbar, K. R., Ligands Effects on the Magnetic Anisotropy of Tetrahedral Cobalt Complexes. *Chem. Commun.* **2014,** *50*, 12266-12269. http://doi.org/10.1039/C4CC05724D

18. Yang, F.; Zhou, Q.; Zhang, Y.; Zeng, G.; Li, G.; Shi, Z.; Wang, B.; Feng, S., Inspiration from Old Molecules: Field-Induced Slow Magnetic Relaxation in Three Air-Stable Tetrahedral Cobalt(ii) Compounds. *Chem. Commun.* **2013,** *49*, 5289-5291. http://doi.org/10.1039/C3CC00277B

19. Boča, R.; Miklovič, J.; Titiš, J., Simple Mononuclear Cobalt(II) Complex: A Single-Molecule Magnet Showing Two Slow Relaxation Processes. *Inorg. Chem.* **2014,** *53*, 2367-2369. https://doi.org/10.1021/ic5000638

20. Ozerov, M.; Bernáth, B.; Kamenskyi, D.; Redlich, B.; van der Meer, A. F. G.; Christianen, P. C. M.; Engelkamp, H.; Maan, J. C., A THz Spectrometer Combining the Free Electron Laser FLARE with 33 T Magnetic Fields. *Appl. Phys. Lett.* **2017,** *110*, 094106. http://doi.org/10.1063/1.4977862

21. Zvyagin, S. A.; Ozerov, M.; Čižmár, E.; Kamenskyi, D.; Zherlitsyn, S.; Herrmannsdörfer, T.; Wosnitza, J.; Wünsch, R.; Seidel, W., Terahertz-Range Free-Electron Laser Electron Spin Resonance Spectroscopy: Techniques and Applications in High Magnetic Fields. *Rev. Sci. Instrum.* **2009,** *80*, 073102. https://doi.org/10.1063/1.3155509

22. Krzystek, J.; Zvyagin, S. A.; Ozarowski, A.; Fiedler, A. T.; Brunold, T. C.; Telser, J., Definitive Spectroscopic Determination of Zero-Field Splitting in High-Spin Cobalt(II). *J. Am. Chem. Soc.* **2004,** *126*, 2148-2155. https://doi.org/10.1021/ja039257y

23. Rechkemmer, Y.; Breitgoff, F. D.; van der Meer, M.; Atanasov, M.; Hakl, M.; Orlita, M.; Neugebauer, P.; Neese, F.; Sarkar, B.; van Slageren, J., A Four-Coordinate Cobalt(II) Single-Ion Magnet with Coercivity and a Very High Energy Barrier. *Nat. Commun.* **2016,** *7*, 10467. http://doi.org/10.1038/ncomms10467

24. Liu, J.-J.; Meng, Y.-S.; Hlavička, I.; Orlita, M.; Jiang, S.-D.; Wang, B.-W.; Gao, S., Determination of zero-field splitting in Co^{2+} halide complexes with magnetic and far-IR measurements. *Dalton Transactions* **2017,** *46*, 7408-7411. http://dx.doi.org/10.1039/C7DT01486D

25. Moseley, D. H.; Stavretis, S. E.; Thirunavukkuarasu, K.; Ozerov, M.; Cheng, Y.; Daemen, L. L.; Ludwig, J.; Lu, Z.; Smirnov, D.; Brown, C. M.; Pandey, A.; Ramirez-Cuesta, A. J.; Lamb, A. C.; Atanasov, M.; Bill, E.; Neese, F.; Xue, Z.-L., Spin–Phonon Couplings in Transition Metal Complexes with Slow Magnetic Relaxation. *Nat. Commun.* **2018,** *9*, 2572. https://doi.org/10.1038/s41467-018-04896-0

26. Moseley, D. H.; Stavretis, S. E.; Zhu, Z.; Guo, M.; Brown, C. M.; Ozerov, M.; Cheng, Y.; Daemen, L. L.; Richardson, R.; Knight, G.; Thirunavukkuarasu, K.; Ramirez-Cuesta, A. J.; Tang, J.; Xue, Z.-L., Inter-Kramers Transitions and Spin–Phonon Couplings in a Lanthanide-Based Single-Molecule Magnet. *Inorg. Chem.* **2020,** *59*, 5218-5230. https://doi.org/10.1021/acs.inorgchem.0c00523

27. Landart-Gereka, A.; Quesada-Moreno, M. M.; Díaz-Ortega, I. F.; Nojiri, H.; Ozerov, M.; Krzystek, J.; Palacios, M. A.; Colacio, E., Large easy-axis magnetic anisotropy in a series of trigonal prismatic mononuclear cobalt(II) complexes with zero-field hidden single-molecule magnet behaviour: The important role of the distortion of the coordination sphere and intermolecular interactions in the slow relaxation. *Inorg. Chem. Front.* **2022,** *9*, 2810-2831. http://dx.doi.org/10.1039/D2QI00275B

28. Rechkemmer, Y.; Fischer, J. E.; Marx, R.; Dörfel, M.; Neugebauer, P.; Horvath, S.; Gysler, M.; Brock-Nannestad, T.; Frey, W.; Reid, M. F.; van Slageren, J., Comprehensive

Spectroscopic Determination of the Crystal Field Splitting in an Erbium Single-ion Magnet. *J. Am. Chem. Soc.* **2015,** *137*, 13114-13120. http://doi.org/10.1021/jacs.5b08344

29. Ray, K.; Begum, A.; Weyhermüller, T.; Piligkos, S.; van Slageren, J.; Neese, F.; Wieghardt, K., The Electronic Structure of the Isoelectronic, Square-Planar Complexes $[Fe^{II}(L)_2]^{2-}$ and $[Co^{III}(LBu)_2]^{-}$ (L^{2-} and $(LBu)^{2-}$ = Benzene-1,2-dithiolates): An Experimental and Density Functional Theoretical Study. *J. Am. Chem. Soc.* **2005,** *127*, 4403-4415. http://doi.org/10.1021/ja042803i

30. Brackett, G. C.; Richards, P. L.; Caughey, W. S., Far-Infrared Magnetic Resonance in Fe(III) and Mn(III) Porphyrins, Myoglobin, Hemoglobin, Ferrichrome A, and Fe(III) Dithioncarbamates. *J. Chem. Phys.* **1971,** *54*, 4383-4401. https://doi.org/10.1063/1.1674688

31. Stavretis, S. E.; Atanasov, M.; Podlesnyak, A. A.; Hunter, S. C.; Neese, F.; Xue, Z.-L., Magnetic Transitions in Iron Porphyrin Halides by Inelastic Neutron Scattering and Ab Initio Studies of Zero-Field Splittings. *Inorg. Chem.* **2015,** *54*, 9790-9801. https://doi.org/10.1021/acs.inorgchem.5b01505

32. Bone, A. N.; Widener, C. N.; Moseley, D. H.; Liu, Z.; Lu, Z.; Cheng, Y.; Daemen, L. L.; Ozerov, M.; Telser, J.; Thirunavukkuarasu, K.; Smirnov, D.; Greer, S. M.; Hill, S.; Krzystek, J.; Holldack, K.; Aliabadi, A.; Schnegg, A.; Dunbar, K. R.; Xue, Z.-L., Applying Unconventional Spectroscopies to the Single-Molecule Magnets, $Co(PPh_3)_2X_2$ (X = Cl, Br, I): Unveiling Magnetic Transitions and Spin-Phonon Coupling. *Chem. Eur. J.* **2021,** *27*, 11110-11125. https://doi.org/10.1002/chem.202100705

33. Kumar, P.; SantaLucia, D. J.; Kaniewska-Laskowska, K.; Lindeman, S. V.; Ozarowski, A.; Krzystek, J.; Ozerov, M.; Telser, J.; Berry, J. F.; Fiedler, A. T., Probing the Magnetic

Anisotropy of Co(II) Complexes Featuring Redox-Active Ligands. *Inorg. Chem.* **2020,** *59*, 16178-16193. https://doi.org/10.1021/acs.inorgchem.0c01812

34. Vallejo, J.; Viciano-Chumillas, M.; Lloret, F.; Julve, M.; Castro, I.; Krzystek, J.; Ozerov, M.; Armentano, D.; De Munno, G.; Cano, J., Coligand Effects on the Field-Induced Double Slow Magnetic Relaxation in Six-Coordinate Cobalt(II) Single-Ion Magnets (SIMs) with Positive Magnetic Anisotropy. *Inorg. Chem.* **2019,** *58*, 15726-15740. https://doi.org/10.1021/acs.inorgchem.9b01719

35. Tin, P.; Stavretis, S. E.; Ozerov, M.; Krzystek, J.; Ponomaryov, A. N.; Zvyagin, S. A.; Wosnitza, J.; Chen, C.-C.; Chen, P. P. Y.; Telser, J.; Xue, Z.-L., Advanced Magnetic Resonance Studies of Tetraphenylporphyrinatoiron(III) Halides. *Appl. Magn. Reson.* **2020,** *51*, 1411-1432. https://doi.org/10.1007/s00723-020-01236-8

36. Gnezdilov, V. P.; Eremenko, V. V.; Peschansky, A. V.; Fomin, V. I., Raman Scattering by Low-Energy Electronic Excitations of Fe^{2+} Ions in Ferrous Fluosilicate. *Fiz. Nizk. Temp. (Low. Temp. Phys.)* **1991,** *17*, 253-258. https://fnt.ilt.kharkov.ua/join.php?fn=/fnt/pdf/17/17-2/f17-0253r.pdf

37. Clark, R. J. H.; Dines, T. J., Electronic Raman Spectroscopy in *Advances in Infrared and Raman Spectroscopy*, **1982**, *9*, 282-360. 1982.

38. Long, D. A., *The Raman Effect. A Unified Treatment of the Theory of Raman Scattering by Molecules. Ch. 9, "Normal and Resonance Electronic and Vibronic Raman Scattering," pp. 289-302*. 2002; Wiley: West Sussex, UK. https://www.wiley.com/en-us/The+Raman+Effect%3A+A+Unified+Treatment+of+the+Theory+of+Raman+Scattering+by+Molecules-p-9780471490289

39. Furrer, A.; Waldmann, O., Magnetic cluster excitations. *Rev. Mod. Phys.* **2013,** *85*, 367-420. https://doi.org/10.1103/RevModPhys.85.367

40. Mitchell, P. C. H.; Parker, S. F.; Ramirez-Cuesta, A. J.; Tomkinson, J., *Vibrational Spectroscopy with Neutrons: With Applications in Chemistry, Biology, Materials Science and Catalysis*. Series on Neutron Techniques and Applications: 2005; World Scientific Publishing Company. https://www.worldscientific.com/worldscibooks/10.1142/5628

41. Dunstan, M. A.; Mole, R. A.; Boskovic, C., Inelastic Neutron Scattering of Lanthanoid Complexes and Single-Molecule Magnets. *Eur. J. Inorg. Chem.* **2019,** *2019*, 1090-1105. https://doi.org/10.1002/ejic.201801306

42. Xue, Z.-L.; Ramirez-Cuesta, A. J.; Brown, C. M.; Calder, S.; Cao, H.; Chakoumakos, B. C.; Daemen, L. L.; Huq, A.; Kolesnikov, A. I.; Mamontov, E.; Podlesnyak, A. A.; Wang, X., Neutron Instruments for Research in Coordination Chemistry. *Eur. J. Inorg. Chem.* **2019,** *2019*, 1065-1089. https://doi.org/10.1002/ejic.201801076

43. Basler, R.; Sieber, A.; Chaboussant, G.; Güdel, H. U.; Chakov, N. E.; Soler, M.; Christou, G.; Desmedt, A.; Lechner, R., Inelastic Neutron Scattering Study of Electron Reduction in Mn12 Derivatives. *Inorg. Chem.* **2005,** *44*, 649-653. https://doi.org/10.1021/ic048931p

44. Bonde, N. A.; Appel, M.; Ollivier, J.; Weihe, H.; Bendix, J., Unequal sensitivities of energy levels in a high-symmetry Ho^{3+} complex towards lattice distortions. *Chem. Commun.* **2022,** *58*, 7431-7434. http://dx.doi.org/10.1039/D2CC02068H

45. Ansbro, S.; Moreno-Pineda, E.; Yu, W.; Ollivier, J.; Mutka, H.; Ruben, M.; Chiesa, A., Magnetic properties of transition metal dimers probed by inelastic neutron scattering. *Dalton Trans.* **2018,** *47*, 11953-11959. http://doi.org/10.1039/C8DT02570C

46. Pinkowicz, D.; Southerland, H. I.; Avendaño, C.; Prosvirin, A.; Sanders, C.; Wernsdorfer, W.; Pedersen, K. S.; Dreiser, J.; Clérac, R.; Nehrkorn, J.; Simeoni, G. G.; Schnegg, A.; Holldack, K.; Dunbar, K. R., Cyanide Single-Molecule Magnets Exhibiting Solvent Dependent Reversible "On" and "Off" Exchange Bias Behavior. *J. Am. Chem. Soc.* **2015,** *137*, 14406-14422. https://doi.org/10.1021/jacs.5b09378

47. Colacio, E.; Ruiz, J.; Ruiz, E.; Cremades, E.; Krzystek, J.; Carretta, S.; Cano, J.; Guidi, T.; Wernsdorfer, W.; Brechin, E. K., Slow Magnetic Relaxation in a Co^{II}–Y^{III} Single-Ion Magnet with Positive Axial Zero-Field Splitting. *Angew. Chem. In. Ed.* **2013,** *52*, 9130-9134. https://doi.org/10.1002/anie.201304386

48. Stavretis, S. E.; Moseley, D. H.; Fei, F.; Cui, H.-H.; Cheng, Y.; Podlesnyak, A. A.; Wang, X.; Daemen, L. L.; Hoffmann, C. M.; Ozerov, M.; Lu, Z.; Thirunavukkuarasu, K.; Smirnov, D.; Chang, T.; Chen, Y.-S.; Ramirez-Cuesta, A. J.; Chen, X.-T.; Xue, Z.-L., Spectroscopic Studies of the Magnetic Excitation and Spin-Phonon Couplings in a Single-Molecule Magnet. *Chem. Eur. J.* **2019,** *25*, 15846-15857. https://doi.org/10.1002/chem.201903635

49. Stavretis, S. E.; Cheng, Y.; Daemen, L. L.; Brown, C. M.; Moseley, D. H.; Bill, E.; Atanasov, M.; Ramirez-Cuesta, A. J.; Neese, F.; Xue, Z.-L., Probing Magnetic Excitations in Co^{II} Single-Molecule Magnets by Inelastic Neutron Scattering. *Eur. J. Inorg. Chem.* **2019,** *2019*, 1119-1127. https://doi.org/10.1002/ejic.201801088

50. Chen, L.; Cui, H.-H.; Stavretis, S. E.; Hunter, S. C.; Zhang, Y.-Q.; Chen, X.-T.; Sun, Y.-C.; Wang, Z.; Song, Y.; Podlesnyak, A. A.; Ouyang, Z.-W.; Xue, Z.-L., Slow Magnetic Relaxations in Cobalt(II) Tetranitrate Complexes. Studies of Magnetic Anisotropy by

Inelastic Neutron Scattering and High-Frequency and High-Field EPR Spectroscopy. *Inorg. Chem.* **2016,** *55*, 12603-12617. https://doi.org/10.1021/acs.inorgchem.6b01544

51. Hunter, S. C.; Podlesnyak, A. A.; Xue, Z.-L., Magnetic Excitations in Metalloporphyrins by Inelastic Neutron Scattering: Determination of Zero-Field Splittings in Iron, Manganese, and Chromium Complexes. *Inorg. Chem.* **2014,** *53*, 1955-1961. https://doi.org/10.1021/ic4028354

52. Bone, A. N.; Stavretis, S. E.; Krzystek, J.; Liu, Z.; Chen, Q.; Gai, Z.; Wang, X.; Steren, C. A.; Powers, X. B.; Podlesnyak, A. A.; Chen, X.-T.; Telser, J.; Zhou, H.; Xue, Z.-L., Manganese tetraphenylporphyrin bromide and iodide. Studies of structures and magnetic properties. *Polyhedron* **2020,** *184*, 114488. https://doi.org/10.1016/j.poly.2020.114488

53. Baker, M. L.; Blundell, S. J.; Domingo, N.; Hill, S., Spectroscopy Methods for Molecular Nanomagnets (in Molecular Nanomagnets and Related Phenomen; Gao, S., Ed., Springer). *Struct. Bond.* **2015,** *164*, 231-291. https://doi.org/10.1007/430_2014_155

54. Singh, A.; Shrivastava, K. N., Optical-Acoustic Two-Phonon Relaxation in Spin Systems. *Phys. Status Solid B* **1979,** *95*, 273-277. https://doi.org/10.1002/pssb.2220950131

55. Świtlicka, A.; Machura, B.; Penkala, M.; Bieńko, A.; Bieńko, D. C.; Titiš, J.; Rajnák, C.; Boča, R.; Ozarowski, A.; Ozerov, M., Slow Magnetic Relaxation in Cobalt(II) Field-Induced Single-Ion Magnets with Positive Large Anisotropy. *Inorg. Chem.* **2018,** *57*, 12740-12755. https://doi.org/10.1021/acs.inorgchem.8b01906

56. Czap, G.; Wagner, P. J.; Li, J.; Xue, F.; Yao, J.; Wu, R.; Ho, W., Detection of Spin-Vibration States in Single Magnetic Molecules. *Phys. Rev. Lett.* **2019,** *123*, 106803. http://doi.org/10.1103/PhysRevLett.123.106803

57. Goodwin, C. A. P.; Ortu, F.; Reta, D.; Chilton, N. F.; Mills, D. P., Molecular Magnetic Hysteresis at 60 Kelvin in Dysprosocenium. *Nature* **2017,** *548*, 439-442. https://doi.org/10.1038/nature23447

58. Lunghi, A.; Totti, F.; Sanvito, S.; Sessoli, R., Intra-Molecular Origin of the Spin-Phonon Coupling in Slow-Relaxing Molecular Magnets. *Chem. Sci.* **2017,** *8*, 6051-6059. http://doi.org/10.1039/C7SC02832F

59. Escalera-Moreno, L.; Suaud, N.; Gaita-Ariño, A.; Coronado, E., Determining Key Local Vibrations in the Relaxation of Molecular Spin Qubits and Single-Molecule Magnets. *J. Phys. Chem. Lett.* **2017,** *8*, 1695-1700. https://doi.org/10.1021/acs.jpclett.7b00479

60. Lunghi, A.; Totti, F.; Sessoli, R.; Sanvito, S., The role of anharmonic phonons in under-barrier spin relaxation of single molecule magnets. *Nat. Commun.* **2017,** *8*, 14620. https://doi.org/10.1038/ncomms14620

61. Escalera-Moreno, L.; Baldoví, J. J.; Gaita-Ariño, A.; Coronado, E., Spin states, vibrations and spin relaxation in molecular nanomagnets and spin qubits: a critical perspective. *Chem. Sci.* **2018,** *9*, 3265-3275. http://doi.org/10.1039/C7SC05464E

62. Ho, L. T. A.; Chibotaru, L. F., Spin-lattice relaxation of magnetic centers in molecular crystals at low temperature. *Phys. Rev. B* **2018,** *97*, 024427. http://doi.org/10.1103/PhysRevB.97.024427

63. Mirzoyan, R.; Hadt, R. G., The dynamic ligand field of a molecular qubit: decoherence through spin–phonon coupling. *Phys. Chem. Chem. Phys.* **2020,** *22*, 11249-11265. http://doi.org/10.1039/D0CP00852D

64. Higdon, N. J.; Barth, A. T.; Kozlowski, P. T.; Hadt, R. G., Spin–phonon coupling and dynamic zero-field splitting contributions to spin conversion processes in iron(II) complexes. *J. Chem. Phys.* **2020,** *152*, 204306. http://doi.org/10.1063/5.0006361

65. Aravena, D.; Ruiz, E., Spin dynamics in single-molecule magnets and molecular qubits. *Dalton Trans.* **2020,** *49*, 9916-9928. http://doi.org/10.1039/D0DT01414A

66. Higdon, N. J.; Barth, A. T.; Kozlowski, P. T.; Hadt, R. G., Spin–phonon coupling and dynamic zero-field splitting contributions to spin conversion processes in iron(II) complexes. *J. Chem. Phys.* **2020,** *152*, 204306. https://aip.scitation.org/doi/abs/10.1063/5.0006361

67. Pilbrow, J. R., Effective *g* values for $S = 3/2$ and $S = 5/2$. *J. Magn. Reson.* **1978,** *31*, 479-490. http://www.sciencedirect.com/science/article/pii/S0022236478800158

68. Gast, P.; Groenen, E. J. J., EPR Interactions – *g*-Anisotropy. *eMagRes* **2016,** *5*, 1435–1444.

69. Jacobs, P. W. M., *Group Theory with Applications in Chemical Physics*. 2005; Cambridge University Press: p 462. https://doi.org/10.1017/CBO9780511535390

70. Koster, G. F.; Dimmock, J. O.; Wheeler, R. G.; Statz, H., *Properties of the Thirty-Two Point Groups*. 1963; MIT Press: Cambridge, MA.

71. Cohen-Tannoudji, C.; Laloe, F.; Diu, B., *Quantum Mechanics*. Vol. 1, 1977; Wiley: New York. https://www.wiley.com/en-ae/Quantum+Mechanics%2C+Volume+1%3A+Basic+Concepts%2C+Tools%2C+and+Applications%2C+2nd+Edition-p-9783527345533#content-section

72. Raman magneto-spectroscopic (RaMS) facilities at NHFML: https://nationalmaglab.org/user-facilities/dc-field/dcfield-techniques/raman-dc.

73. Gómez-Coca, S.; Urtizberea, A.; Cremades, E.; Alonso, P. J.; Camón, A.; Ruiz, E.; Luis, F., Origin of slow magnetic relaxation in Kramers ions with non-uniaxial anisotropy. *Nat. Commun.* **2014,** *5*, 4300. https://doi.org/10.1038/ncomms5300

74. VISION (Vibrational Spectrometer) at ORNL: https://neutrons.ornl.gov/vision.

75. DCS (Disk Chopper Spectrometer) at NCNR: https://www.nist.gov/ncnr/dcs-disk-chopper-spectrometer.

76. Schönherr, T.; Atanasov, M.; Adamsky, H., Angular Overlap Model. In *Comprehensive Coordination Chemistry II*, McCleverty, J. A.; Meyer, T. J., Eds. Pergamon: Oxford, 2003; pp 443-455. https://doi.org/10.1016/B0-08-043748-6/01052-5

77. Lang, L.; Atanasov, M.; Neese, F., Improvement of Ab Initio Ligand Field Theory by Means of Multistate Perturbation Theory. *J. Phys. Chem. A* **2020,** *124*, 1025-1037. https://doi.org/10.1021/acs.jpca.9b11227

78. Tomlinson, A. A. G.; Bellitto, C.; Piovesana, O.; Furlani, C., Crystal Polarised Spectra, and Electronic Structures, of Some Pseudotetrahedral Cobalt(II) Complexes with 'Soft' Bonding Ligands. *J. Chem. Soc., Dalton Trans.* **1972**, 350-354. http://dx.doi.org/10.1039/DT9720000350

79. Davies, J. E.; Gerloch, M.; Phillips, D. J., Phosphine π-acceptor properties in dihalogenobis(triphenylphosphine)-nickel(II) and -cobalt(II). *J. Chem.Soc., Dalton Trans.* **1979**, 1836-1842. http://dx.doi.org/10.1039/DT9790001836

80. Togo, A., VASP & phonopy calculation. http://phonopy.github.io/phonopy/vasp.html

81. Alternatively, having determined experimentally or theoretically these parameters, D_{xx}, D_{yy}, and D_{zz} are given by $D_{xx} = E - (1/2)D$, $D_{yy} = -E - (1/2)D$, $D_{zz} = (2/3)D$.

82. Krzystek, J.; Smirnov, D.; Schlegel, C.; van Slageren, J.; Telser, J.; Ozarowski, A., High-Frequency and -Field EPR and FDMRS Study of the $[Fe(H_2O)_6]^{2+}$ Ion in Ferrous Fluorosilicate. *J. Magn. Reson.* **2011,** *213*, 158-165. http://doi.org/10.1016/j.jmr.2011.09.046

83. FIRMS facilities at NHMFL: https://nationalmaglab.org/user-facilities/dc-field/dcfield-techniques/magneto-optics-ir-thz-dc.

84. CNCS (Cold Neutron Chopper Spectrometer) at ORNL: https://neutrons.ornl.gov/cncs.

85. Xue, Z.-L.; Ramirez-Cuesta, A. J.; Brown, C. M.; Calder, S.; Cao, H.; Chakoumakos, B. C.; Daemen, L. L.; Huq, A.; Kolesnikov, A. I.; Mamontov, E.; Podlesnyak, A. A.; Wang, X., Neutron Instruments for Research in Coordination Chemistry. *Eur. J. Inorg. Chem.* **2019**, 1065-1089. https://doi.org/10.1002/ejic.201801076

86. Krzystek, J.; Ozarowski, A.; Telser, J., Multi-frequency, high-field EPR as a powerful tool to accurately determine zero-field splitting in high-spin transition metal coordination complexes. *Coord. Chem. Rev.* **2006,** *250*, 2308-2324. https://doi.org/10.1016/j.ccr.2006.03.016

87. Roessler, M. M.; Salvadori, E., Principles and applications of EPR spectroscopy in the chemical sciences. *Chem. Soc. Rev.* **2018,** *47*, 2534-2553. http://dx.doi.org/10.1039/C6CS00565A

88. Rizzi, A. C.; Neuman, N. I.; González, P. J.; Brondino, C. D., EPR as a Tool for Study of Isolated and Coupled Paramagnetic Centers in Coordination Compounds and Macromolecules of Biological Interest (Eur. J. Inorg. Chem. 2/2016). *Eur. J. Inorg. Chem.* **2016,** *2016*. https://doi.org/10.1002/ejic.201690002

89. Chilton, N. F.; Anderson, R. P.; Turner, L. D.; Soncini, A.; Murray, K. S., PHI: A powerful new program for the analysis of anisotropic monomeric and exchange-coupled polynuclear d- and f-block complexes. *J. Comput. Chem.* **2013,** *34*, 1164-1175. https://doi.org/10.1002/jcc.23234

90. Copley, J. R. D.; Cook, J. C., The Disk Chopper Spectrometer at NIST: A New Instrument for Quasielastic Neutron Scattering Studies. *Chem. Phys.* **2003,** *292*, 477-485. https://doi.org/10.1016/S0301-0104(03)00124-1

91. Seeger, P. A.; Daemen, L. L.; Larese, J. Z., Resolution of VISION, a Crystal-Analyzer Spectrometer. *Nucl. Instr. Meth. Phys. Res. A* **2009,** *604*, 719-728. http://doi.org/10.1016/j.nima.2009.03.204

92. Neese, F., Software update: the ORCA program system, version 4.0. *WIREs Comput. Mol. Sci.* **2018,** *8*, e1327. https://doi.org/10.1002/wcms.1327

93. Neese, F.; Wennmohs, F.; Becker, U.; Riplinger, C., The ORCA quantum chemistry program package. *J. Chem. Phys.* **2020,** *152*, 224108. http://doi.org/10.1063/5.0004608

94. Roos, B. O.; Taylor, P. R.; Sigbahn, P. E. M., A complete active space SCF method (CASSCF) using a density matrix formulated super-CI approach. *Chem. Phys.* **1980,** *48*, 157-173. https://doi.org/10.1016/0301-0104(80)80045-0

95. Hess, B. A., Relativistic electronic-structure calculations employing a two-component no-pair formalism with external-field projection operators. *Phys. Rev. A* **1986,** *33*, 3742-3748. http://doi.org/10.1103/PhysRevA.33.3742

96. Weigend, F., Accurate Coulomb-fitting basis sets for H to Rn. *Phys. Chem. Chem. Phys.* **2006,** *8*, 1057-1065. http://doi.org/10.1039/B515623H

97. Weigend, F.; Ahlrichs, R., Balanced basis sets of split valence, triple zeta valence and quadruple zeta valence quality for H to Rn: Design and assessment of accuracy. *Phys. Chem. Chem. Phys.* **2005,** *7*, 3297-3305. http://doi.org/10.1039/B508541A

98. Noro, T.; Sekiya, M.; Koga, T., Segmented contracted basis sets for atoms H through Xe: Sapporo-(DK)-nZP sets (n = D, T, Q). *Theor. Chem. Acc.* **2012,** *131*, 1124. https://doi.org/10.1007/s00214-012-1124-z

99. Angeli, C.; Cimiraglia, R.; Evangelisti, S.; Leininger, T.; Malrieu, J.-P., Introduction of n-electron valence states for multireference perturbation theory. **2001,** *114*, 10252-10264. https://aip.scitation.org/doi/abs/10.1063/1.1361246

100. Angeli, C.; Cimiraglia, R.; Malrieu, J.-P., N-electron valence state perturbation theory: a fast implementation of the strongly contracted variant. *Chem. Phys. Lett.* **2001,** *350*, 297-305. https://doi.org/10.1016/S0009-2614(01)01303-3

101. Angeli, C.; Cimiraglia, R.; Malrieu, J.-P., n-electron valence state perturbation theory: A spinless formulation and an efficient implementation of the strongly contracted and of the partially contracted variants. **2002,** *117*, 9138-9153. https://aip.scitation.org/doi/abs/10.1063/1.1515317

102. Atanasov, M. G., D.; Sivalingam, K.; Neese, F., A Modern First-Principles View on Ligand Field Theory Through the Eyes of Correlated Multireference Wavefunctions. In *Molecular Electronic Structures of Transition Metal Complexes II*, Mingos, D. M. P.; Day, P.; Dahl, J. P., Eds. Springer Berlin Heidelberg: Berlin, Heidelberg, 2012; pp 149-220. https://doi.org/10.1007/430_2011_57

103. Singh, S. K.; Eng, J.; Atanasov, M.; Neese, F., Covalency and chemical bonding in transition metal complexes: An ab initio based ligand field perspective. *Coord. Chem. Rev.* **2017,** *344*, 2-25. https://doi.org/10.1016/j.ccr.2017.03.018

104. Pedersen, K. S.; Woodruff, D. N.; Singh, S. K.; Tressaud, A.; Durand, E.; Atanasov, M.; Perlepe, P.; Ollefs, K.; Wilhelm, F.; Mathonière, C.; Neese, F.; Rogalev, A.; Bendix, J.; Clérac, R., $[OsF_6]^{x-}$: Molecular Models for Spin-Orbit Entangled Phenomena. *Chem. Eur. J.* **2017,** *23*, 11244-11248. https://doi.org/10.1002/chem.201702894

105. Kresse, G.; Furthmüller, J., Efficient Iterative Schemes for Ab initio Total-Energy Calculations using a Plane-Wave Basis Set. *Phys. Rev. B* **1996,** *54*, 11169-11186. https://doi.org/10.1103/PhysRevB.54.11169

106. Kresse, G.; Joubert, D., From Ultrasoft Pseudopotentials to the Projector Augmented-Wave Method. *Phys. Rev. B* **1999,** *59*, 1758-1775. https://doi.org/10.1103/PhysRevB.59.1758

107. Blöchl, P. E., Projector Augmented-Wave Method. *Phys. Rev. B* **1994,** *50*, 17953-17979. https://doi.org/10.1103/PhysRevB.50.17953

108. Perdew, J. P.; Burke, K.; Ernzerhof, M., Generalized Gradient Approximation Made Simple. *Phys. Rev. Lett.* **1996,** *77*, 3865-3868. https://doi.org/10.1103/PhysRevLett.77.3865

109. Klimeš, J.; Bowler, D. R.; Michaelides, A., Chemical Accuracy for the Van der Waals Density Functional. *J. Phys. Condens. Matter* **2010,** *22*, 022201. https://doi.org/10.1088/0953-8984/22/2/022201

110. Togo, A.; Tanaka, I., First Principles Phonon Calculations in Materials Science. *Scr. Mater.* **2015,** *108*, 1-5. http://doi.org/10.1016/j.scriptamat.2015.07.021

Tables of Contents Synopsis & Graphic

Zero-field splitting (ZFS) in $Co(AsPh_3)_2I_2$, a single-molecule magnet (SMM), has been probed by inelastic neutron scattering, far-IR magneto- and Raman magneto-spectroscopies, and electronic calculations, revealing $2D' = 54\ cm^{-1}$. Spin-phonon couplings as avoided crossings have been observed in both Raman (*g* modes) and far-IR (*u* modes) spectroscopies. The phonon modes and their symmetries have been assigned through DFT calculations. Features of different techniques to determine ZFS and other parameters are summarized.